Collision Resilient Insect-Scale Soft-Actuated Aerial Robots With High Agility

YuFeng Chen, *Member, IEEE*, Siyi Xu, *Student Member, IEEE*, Zhijian Ren, *Student Member, IEEE*, and Pakpong Chirarattananon, *Member, IEEE*

***Abstract*—Flying insects are remarkably agile and robust. As they fly through cluttered natural environments, they can demonstrate aggressive acrobatic maneuvers such as backflip, rapid escape, and in-flight collision recovery. Current state-of-the-art subgram microaerial-vehicles (MAVs) are predominately powered by rigid actuators such as piezoelectric ceramics, but they have low fracture strength (120 MPa) and failure strain (0.3%). Although these existing systems can achieve a high lift-to-weight ratio, they have not demonstrated insect-like maneuvers such as somersault or rapid collision recovery. In this article, we present a 665 mg aerial robot that is powered by novel dielectric elastomer actuators (DEA). The new DEA achieves high power density (1.2 kW/kg) and relatively high transduction efficiency (37%). We further incorporate this soft actuator into an aerial robot to demonstrate novel flight capabilities. This insect-scale aerial robot has a large lift-to-weight ratio (>2.2:1) and it achieves an ascending speed of 70 cm/s. In addition to demonstrating controlled hovering flight, it can recover from an in-flight collision and perform a somersault within 0.16 s. This work demonstrates that soft aerial robots can achieve insect-like flight capabilities absent in rigid-powered MAVs, thus showing the potential of a new class of hybrid soft-rigid robots.**

***Index Terms*—Biologically-inspired robots, dielectric elastomer actuators, flapping wing, soft robots.**

I. Introduction

FLYING insects exhibit remarkable agility and robustness when performing tasks such as feeding, evading predators, pollination, and constructing a hive. For instance, a fruit fly turns upside down within 40 ms when it perches inverted on a ceiling [1]. After being hit by a raindrop, a mosquito can quickly recover its stability within 0.2 s [2]. On average, a honeybee's wing collides with its surrounding once every second during the bee's lifetime [3]. Achieving these flight capabilities require an insect's flight muscles to be power dense, controllable, and robust.

Developing agile and robust micro-aerial-vehicles (MAVs) that can demonstrate insect-like flight capabilities poses significant scientific and engineering challenges. On a larger scale (10–200 g), numerous agile rotary vehicles [4]–[7] have been developed to demonstrate aggressive maneuvers such as body flips and banked turns. A fast-spinning rotor can be easily damaged if it collides with an obstacle. To enable rotary vehicles to navigate in highly cluttered environments, previous studies have developed collision-resilient mechanisms such as a rotary protective cage [8], origami-inspired folding flexures [9], and a rotary origami protective system [10], [11]. In recent years, several biologically inspired flapping-wing microaerial-vehicles (FWMAV) have been developed to demonstrate biomimetic flights [12]–[16]. These vehicles have shown animal-like flight capabilities such as rapid banked turns [14], evasive maneuvers [17], collision sensing [12], and collision recovery [18]. There are two major challenges for enabling these flight capabilities in subgram aerial robots. First, the abovementioned mesoscale MAVs are all driven by electromagnetic motors, but their power density and efficiency would substantially reduce if they shrink to a smaller scale (< 1 g, < 1 cm). Consequently, electromagnetic motors are unsuitable for driving subgram aerial robots. Second, adverse surface-area-to-volume scaling implies protective cages become infeasible at a smaller scale. A collision resilient cage will occupy a large fraction ($> 20\%$) of the robot's weight in subgram MAVs.

To overcome the challenge of microscale actuation, several types of microscale actuators have been developed [19]–[21] to power subgram robots. A recent work [19] created a catalytic artificial muscle and used it to construct a power-autonomous crawling robot. Furthermore, polyvinylidene fluoride actuators have been developed to enable agile crawling locomotion in a 64 mg robot [20]. However, most microscale actuators do not have sufficient power density to achieve liftoff flight.

Over the past decade, a new class of power dense and high bandwidth microscale actuators have been developed to construct subgram FWMAVs. Most existing subgram FWMAVs [22]–[30] are powered by piezoelectric actuators, and they have demonstrated controlled flight [22], onboard sensing [23], laser [24], or solar-powered [25] takeoffs, and versatile functions such as perching [26], [27] and hybrid aerial-aquatic

Manuscript received October 16, 2020; accepted December 19, 2020. Date of publication February 18, 2021; date of current version October 1, 2021. This work was supported by the Research Laboratory of Electronics, MIT under the Research Support Committee Grant 2244181. This paper was recommended for publication by Associate Editor M. Rubenstein and Editor M. Yim upon evaluation of the reviewers' comments. *(Corresponding author: YuFeng Chen.)*

YuFeng Chen and Zhijian Ren are with the Soft and Microrobotics Lab, Research Laboratory of Electronics, Department of Electrical Engineering and Computer Science, Massachusetts Institute of Technology, Cambridge, MA 02139 USA (e-mail: yufengc@mit.edu; zhijianr@mit.edu).

Siyi Xu is with the School of Engineering and Applied Sciences, Harvard University, Cambridge, MA 02138 USA (e-mail: sxu1@g.harvard.edu).

Pakpong Chirarattananon is with the Department of Biomedical Engineering, City University of Hong Kong, Hong Kong SAR, China (e-mail: pakpong.c@cityu.edu.hk).

This article has supplementary material provided by the authors and color versions of one or more figures available at https://doi.org/10.1109/TRO.2021.3053647.

Digital Object Identifier 10.1109/TRO.2021.3053647

locomotion [28]. In addition, multiple-wing designs are recently developed [29], [30] to improve flight stability or to reduce fabrication complexity. While these state-of-the-art piezoelectric-powered FWMAVs have achieved impressive flight capabilities, these robots have not demonstrated in-flight collision recovery or aggressive acrobatic maneuvers such as somersaults. This shortcoming is mainly contributed by the actuator's low fracture strength (120 MPa) and failure strain (0.3%). In our previous works [28], [31] on piezoelectric-powered MAVs, we found the actuators are prone to cracking under an impulsive load or large strain. For instance, if a robot wing hits an obstacle during flight, the collisional impact would be transmitted to the actuator through the robot transmission. This impact can easily crack the actuator. As demonstrated in a recent work [18], collision resilience can be improved by constructing bioinspired wings that can buckle under large external loads. While this design is effective for a 17.8 g FWMAV, it is difficult to implement for microscale robots. Another recent work [32] developed a collapsible wing for an 80 mg FWMAV, but it found the robot's net lift reduces by over 30% because the added mechanism substantially increased the wing inertia.

Furthermore, a piezoelectric actuator's low fracture strength also limits the robot's flight capability. Piezoelectric actuators are driven near the system resonant frequency to maximize output mechanical power. If there is a sudden change of control signal (either a large change of frequency or voltage amplitude), the actuator may crack due to the large instantaneous strain. Consequently, it is difficult for piezoelectric-powered FWMAVs to demonstrate aggressive maneuvers or in-flight collision recovery because of the large stress and strain that the actuator needs to endure.

To develop robust and agile insect-scale MAVs, we replaced rigid actuators with dielectric elastomer actuators (DEAs) and demonstrated the first takeoff and controlled flight of a soft-actuated MAV [33]. In addition to demonstrating controlled hovering flight, our previous work showed soft-actuated MAVs can survive collisions, but they are unable to immediately recover from the impact as the robot lift and efficiency were much worse (3 times and 15 times lower) than that of the state-of-the-art piezoelectric-powered MAVs. Besides from achieving hovering flights, our previous robot could not demonstrate new flight capabilities.

In this article, we report the design, fabrication, and control of a new DEA-powered robot (see Fig. 1) with substantial performance improvement and new flight capabilities. Compared to our previous work [33], we present a new DEA whose power density and transduction efficiency are improved by 100% and 560%, respectively. Based on the new DEA, we redesign other robot components and achieve an 83% increase of net robot lift. This substantial improvement of robot lift further enables novel flight capabilities. The new robot can demonstrate in-flight collision recovery and complete a somersault within 0.16 s—flight maneuvers that have not been achieved in rigid-powered subgram MAVs. Furthermore, the robot's vertical ascending speed exceeds 70 cm/s, which makes it among the fastest soft mobile robots and outperforms rigid-powered subgram MAVs. By demonstrating controllable, robust, and agile locomotion in a soft aerial robot, this work shows a novel class of highly dynamic soft robots whose performance are comparable or even superior to their rigid counterparts.

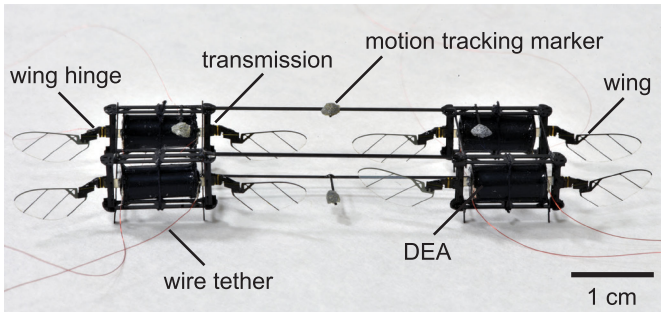

Fig. 1. Perspective view of a 665 mg aerial robot that is powered by DEAs. This robot consists of four identical modules, and each module consists of an airframe, a DEA, a pair of wing hinges, wings, and transmissions. The robot carries four motion trackers to perform closed-loop flights. The robot dimensions are $6 \times 2 \times 1$ cm.

II. Actuator Design and Characterization

The substantial improvement of robot performance is mainly enabled by the development of a new power-dense DEA. In this work, we increase a DEA's power density by 100% through using new elastomeric materials and reducing the electrode resistance. In our previous work [33], our DEA fabrication process was adapted from an existing method [34] that did not optimize output power density and efficiency. Our previous DEA's power density and efficiency were 600 W/kg and 5.6%, and they are 40% and 15 times lower than the performance of piezoelectric actuators at a similar scale [25].

Here, we report a substantial performance improvement by switching to a less viscous elastomeric material Elastosil P7670. In the fabrication process, we reduce the contact resistance to improve transduction efficiency. We show the new DEA achieves a 100% increase of power density and a 560% improvement of efficiency. Details of DEA design, fabrication, and characterization are described in the following sections.

A. Actuator Design, Material Selection, and Fabrication

The DEA consists of a multilayered elastomer sheet that is rolled into a cylinder. The length, width, and thickness of the elastomer sheet are 8 mm, 50 mm, and 210 μm, respectively. After the elastomer is rolled into a cylinder, carbon fiber caps are attached to each end and they serve as both the electrical and mechanical connections. The detailed fabrication process is described in a prior work [33].

The choice of elastomer material has a large influence on a DEA's performance. Most previous studies [35]–[38] investigated the influence of elastomer material properties (i.e., modulus and dielectric constant) on a DEA's output energy density. A DEA consists of an elastomer layer sandwiched between two compliant electrodes, and it can be modeled as a compliant variable capacitor. Under an applied voltage, the Maxwell stress σ induced by the electric field is given by

$$\sigma = \epsilon_0 \epsilon_r E^2 \tag{1}$$

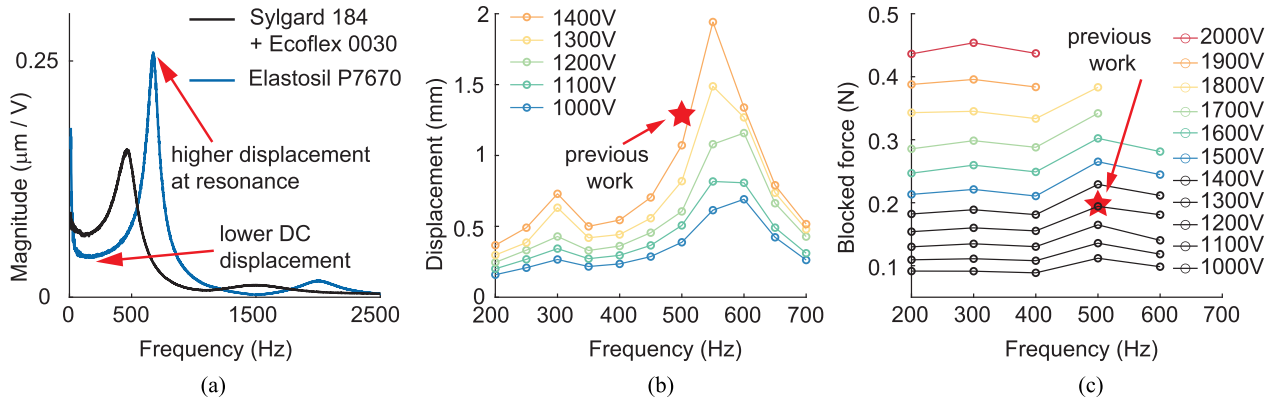

Fig. 2. Resonance, free displacement, and blocked force characterization of the DEA. (a) Frequency response comparison of two DEAs made of different elastomers. The stiffer DEA (Elastosil P7670) has a smaller motion at low frequencies but a higher displacement at resonance. (b)–(c) Free displacement (b) and blocked force (c) as functions of driving frequencies and voltage amplitudes. The maximum displacement and force are improved by 60% and 120% compared to our previous results [33].

where ϵ_0 is the permittivity of free space, ϵ_r is the dielectric constant, and E is the applied electric field. Assuming the DEA actuates in a linearly elastic domain, the output energy density e is given by

$$e = \frac{\sigma^2}{2Y} = \frac{\epsilon_0^2 \epsilon_r^2 E^4}{2Y} \tag{2}$$

where Y is the elastomer's modulus. Equation (2) implies that maximizing energy density requires choosing an elastomer of high dielectric constant, high dielectric strength, and low modulus.

However, this quasi-steady model does not consider a DEA's dynamic response. A DEA's resonant frequency, maximum output power, and its quality factor at resonance are critical performance metrics for achieving flight. While (2) suggests choosing an elastomer of lower modulus can improve energy density, this choice may adversely affect other elastomer properties such as dielectric strength and viscoelasticity. Heuristically softer elastomer has lower dielectric strength and higher viscoelasticity, and these will reduce a DEA's resonant frequency and maximum operating voltage.

We experiment with numerous elastomeric materials and find that an increase of elastomer modulus leads to an increase of power density. Specifically, we compare two DEAs of identical geometry but different elastomers. A DEA is made of the elastomer developed in our previous study (5:4 mixture of Ecoflex 0030 and Sylgard 184) [33], and the elastomer has a modulus of 140 kPa. In addition, another DEA is made of Elastosil P7670, which has a measured modulus of 200 kPa. In Fig. 2(a), we compare the frequency response of the DEA free displacement under an input voltage of 300 V. While the previous elastomer (black line) has higher displacement at low frequencies (< 500 Hz), the new elastomer (blue line) has a higher resonance peak and its resonant frequency increases to approximately 700 Hz. This measurement shows that although Elastosil P7670 has lower static displacement, its dynamic resonance exhibits a much higher quality factor, and therefore, shows a substantially larger displacement at a higher resonant frequency. This implies the new material is more suitable for driving dynamic aerial robots near resonance. Moreover, we find that Elastosil P7670 has a higher dielectric strength compared to the previous material. We measure the dielectric strength of the new material to be greater than 65 V/μm at frequencies larger than 300 Hz. Given the elastomer thickness is approximately 30 μm, the maximum DEA voltage increases from 1.4 kV [33] to around 2 kV.

In addition, we find Elastosil P7670 to be a more suitable material because it accelerates the fabrication process. This elastomer cures in less than 5 min at 60 °C, whereas the previous material requires over 40 min at 70 °C to cure. In our multilayered fabrication process, we need to prepare seven elastomer layers sequentially. Having a substantial reduction of cure time reduces the DEA fabrication time from 6 h to under 2 h. Furthermore, Elastosil P7670 has better bonding with the carbon conductive adhesive (Electron Microscopy Sciences). In the following sections, we report the new DEA's performance and efficiency.

B. *Free Displacement and Blocked Force Characterization*

Here, we report the new DEA's free displacement and blocked force measurements. Similar to our previous work [33], we use a laser vibrometer (Polytec PSV-500) to measure a DEA's displacement. Fig. 2(b) shows the DEA's free displacement amplitude (peak-to-peak value) as a function of driving frequency and voltage. Given the DEA's length is 8 mm, Fig. 2(b) shows the strain reaches 25% (2 mm) when the driving condition is 550 Hz and 1400 V. This exceeds the maximum strain of our previous DEA [red star in Fig. 2(b)] by 60%. For free displacement experiments, we do not drive the DEA with higher voltages because nonlinear effects such as pull-in-instability and period doubling may take place at a large strain. These nonlinear effects introduce large measurement error and reduce the DEA's lifetime. When the DEA is installed into our aerial robot, the aerodynamic load limits the DEA's maximum strain to below 15% at the robot's peak operating conditions.

We further characterize the DEA's blocked force using a Nano17 Titanium force sensor. Fig. 2(c) shows the DEA's blocked force as a function of driving frequency and voltage. Since the DEA is blocked by a sensor, the strain remains 0% in these measurements. Without experiencing a large strain, the

DEA can be driven at higher voltages without experiencing nonlinear effects. Fig. 2(c) shows the maximum blocked force reaches 0.44 N, which represents a 120% improvement over the previous work [red star in Fig. 2(c)]. We use a Trek 677B high voltage amplifier for these experiments, and we are unable to drive the DEA at several high voltage and high frequency operating points because the DEA current exceeds the amplifier's limit.

In summary, this new DEA can be driven at substantially higher voltage and frequency conditions, and it shows markedly higher blocked force and free displacement. In the previous study [33], we estimate a DEA's power density p using the formula:

$$p = \frac{F_B \delta f}{2 m_a} \tag{3}$$

where m_a, F_B, δ, and f are the DEA's mass, blocked force, free displacement, and operating frequency, respectively. Since we cannot drive the new DEA at high voltages to measure its free displacement, we report the DEA's power density based on its operating condition when it is installed into a robot. At the maximum lift condition, the DEA's blocked force, displacement, and driving frequency are 0.44 N, 1.25 mm, and 475 Hz, respectively. The DEA weighs 110 mg, and its power density is calculated to be 1.2 kW/kg. This represents an 100% increase of power density compared to our previous result, and it is comparable to the state-of-the-art piezoelectric actuator at a similar scale [21].

C. Actuator Efficiency

In addition to substantially improving the DEA's power density, we further demonstrate a 560% improvement of transduction efficiency. We design a circuit [see Fig. 3(a)] to measure the DEA's electrical power intake. The DEA is modeled as a resistor and a capacitor connected in series [red box in Fig. 3(a)]. The DEA driving signal V_{IN} is given by

$$V_{IN} = V_I + V_I \cos 2\pi f t \tag{4}$$

where V_I is the voltage amplitude and f is the actuation frequency. We use an oscilloscope (Tektronix TDS3014) to measure the voltage outputs V_1 and V_2. In Fig. 3(a), V_1 and V_2 are measured relative to ground. Based on V_1 and V_2, the DEA voltage and current are calculated as

$$\begin{aligned} i_{\text{DEA}} &= \frac{V_2}{R_3} - \frac{V_1 - V_2}{R_2} \\ v_{\text{DEA}} &= (V_1 - V_2)\left(\frac{R_1 + R_2}{R_2}\right). \end{aligned} \tag{5}$$

Based on the DEA current and voltage, we can calculate the DEA's time averaged power dissipation

$$p_{\text{avg}} = \frac{1}{T}\int_0^T v_{\text{DEA}}(t) \times i_{\text{DEA}}(t) \mathrm{d}t. \tag{6}$$

In addition, we can approximate the DEA voltage and current as

$$\begin{aligned} i_{D,\text{fit}} &\approx I_O \cos(2\pi f t + \phi) \\ v_{D,\text{fit}} &\approx V_O + V_O \cos(2\pi f t) \end{aligned} \tag{7}$$

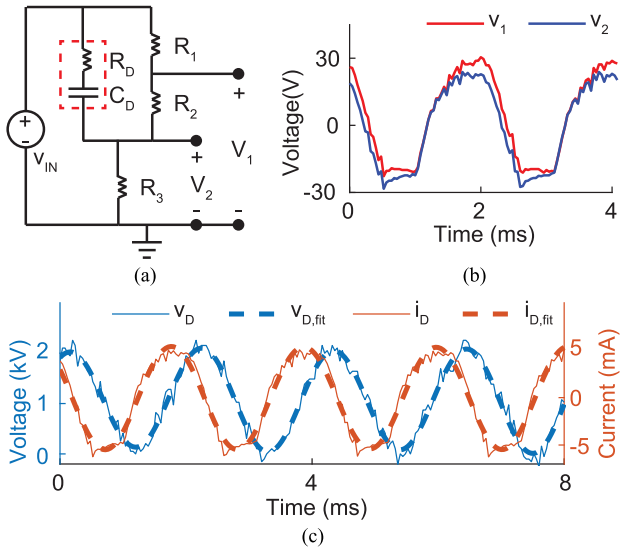

Fig. 3. Characterization of DEA transduction efficiency. (a) We design a circuit to measure the DEA's input power and effective capacitance (C_D) and resistance (R_D). The values of the resistors R_1, R_2, and R_3 are 10 MΩ, 39 kΩ, and 4.7 kΩ, respectively. (b) Measured V_1 and V_2 when the input signal has a maximum value of 2000 V and a frequency of 475 Hz. (c) Measured and fitted DEA voltages and currents. According to the best fit lines, the values of C_D and R_D are calculated to be 1.8 nF and 24 kΩ, respectively.

where the coefficients V_O, I_O, and ϕ are fitted from the data. Since we approximate a DEA as a series RC circuit, the equivalent resistance R_D and capacitance C_D are calculated as

$$\begin{aligned} R_D &= \frac{V_O}{I_O} \frac{1}{\tan\phi\sqrt{1 + 1/\tan^2\phi}} \\ C_D &= \frac{I_O}{2\pi f V_O}\sqrt{1 + 1/\tan^2\phi}. \end{aligned} \tag{8}$$

Fig. 3(b) and (c) shows an experiment in which the robot is operated at its peak operating condition. The input voltage amplitude and driving frequency are 2000 V and 475 Hz, respectively. Fig. 3(b) shows the measured signals V_1 and V_2, and Fig. 3(c) compares the measured and fitted DEA currents and voltages. Based on these measurements, the DEA resistance, capacitance, and average input electrical power are calculated to be 24 kΩ, 1.8 nF, and 0.32 W, respectively. At this driving condition, the DEA's mechanical output power is calculated to be 0.12 W according to (3). Based on these measurements, the DEA's transduction efficiency η is calculated as

$$\eta = \frac{p_{\text{mechanical output}}}{p_{\text{electrical input}}} = 37\%. \tag{9}$$

While previous studies of DEAs [39], [40] have achieved over 90% transduction efficiencies, the DEAs were driven at much lower frequencies (<10 Hz). In contrast, a previous study on dynamic DEAs [41] reports a less than 1% efficiency when the DEA operates at 450 Hz. Similarly, our previous DEA [33] has a low efficiency of 5.6% when it is driven at 300 Hz. In this study, we show that DEAs can achieve a much higher efficiency of 37% at highly dynamic operating conditions (450 Hz). This substantial improvement of transduction efficiency can contribute to future works on developing power autonomous soft-actuated

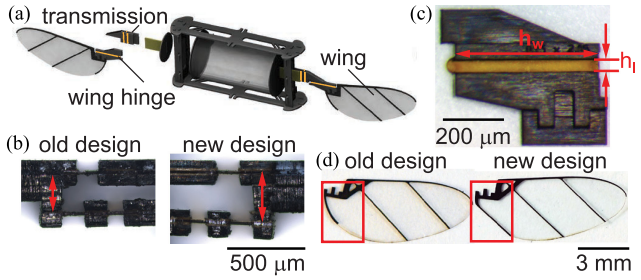

Fig. 4. Robot design and fabrication. (a) CAD image of the robot design. (b) Compared to our previous study, the robot transmission length l_3 (indicated by the red arrows) increases from 400 μm to 500 μm. (c) New robot's wing hinge dimensions are changed to 2.05 mm $\times$ 0.10 mm $\times$ 12.7 μm. (d) New robot wing's inner spar is straightened to improve collision resilience.

aerial robots. The main challenges of achieving power autonomy will be discussed in Section V.

III. Robot Design and Static Characterization

Based on the DEA characterization results, we develop a 164 mg flapping-wing robot that demonstrates substantially improved net lift. Compared to our previous work, the robot operating frequency and net lift increase by 60% and 83%, respectively. In this section, we describe the overall robot design, static flapping-wing experiments, and liftoff experiments.

A. Robot Components Design

This robot has the same overall design as our previous work [33]. As shown in Fig. 4(a), the robot consists of an airframe, transmissions, wing hinges, and wings. The DEA's linear actuation is converted into the robot's wing stroke motion via a linear four-bar transmission. As the robot's wing flaps, the wing passively rotates around the pitch axis and this motion is mediated by the compliant wing hinge.

While this robot shares the same overall design with our previous work, every component is redesigned to accommodate the new DEA. In the previous section, we show the new DEA has an 100% increase of power density, and its stiffness and resonance also increase. The new components are designed based on the methods discussed in our previous studies [31], [33]. Specifically, Fig. 4(b) shows the robot transmission length l_3 is increased from 400 to 500 μm. Fig. 4(c) illustrates the hinge dimensions h_w and h_l are adjusted to 2.05 and 0.10 mm, respectively. The hinge is made of a polyimide film that is 12.7 μm thick. The new DEA, robot transmissions, and wing hinges lead to a substantial improvement of the robot's net lift. Robot flapping experiments are described in Section III-B.

We further improve the wing design so it can operate under larger aerodynamic loads and survive collisions. We use a new type of carbon fiber (Tohotenax QA112-0250) to improve the wing stiffness because it needs to generate larger forces. Fig. 4(d) further shows the wing is modified near its wing root position. The inner spar is changed from a curved design into a straight segment. This design change improves the wing's collision robustness. The wing leading edge spar and diagonal spars align with the carbon fiber's directions to enhance stiffness. In our previous study [33] on robot collision resilience, the inner wing spar [illustrated by red rectangles in Fig. 4(d)] may break if it collides with an obstacle. Straightening the wing inner spar makes it more resilient against collisions. This is crucial for enabling new demonstrations such as in-flight collision recovery and somersaults, which will be described in Section IV.

B. Robot Flapping-Kinematics

We conduct static flapping-wing experiments to characterize wing kinematics and performance. Supplementary Video 1 shows a sample flapping wing experiment, and Fig. 5(a) illustrates half of a flapping cycle. The robot is driven with a sinusoidal signal whose amplitude and frequency are 2000 V and 450 Hz, respectively. The flapping-wing kinematics have two degrees-of-freedom (DOF)—wing stroke and passive pitch motion. Fig. 5(a) illustrates these two DOFs. Using an existing motion tracking method [33], we track the wing stroke and pitch motion of the left and the right wings [see Fig. 5(b)]. At this operating condition, the stroke amplitudes (red) of the left and the right wings are 71° and 69°, respectively. The pitching amplitudes (blue) of the left and the right wings are 119° and 117°, respectively. Compared to our previous work [33], the robot's flapping frequency increases from 280 to 450 Hz. This flapping frequency is the highest among all flapping-wing robots, further showing soft actuators can be power dense and high bandwidth. According to a quasi-steady model [31], the robot's mean lift force is proportional to the square of the flapping frequency, and this scaling relationship predicts an over two times increase of net lift.

We further characterize the robot's flapping-wing kinematics at different operating voltages and frequencies. Fig. 5(c) shows the robot's wing stroke amplitude as functions of frequencies and voltages. The robot's peak stroke amplitude is 78° at the operating condition 2000 V and 480 Hz. In Section III-C, we describe liftoff tests that measure the robot's net lift force.

C. Mean Lift Force Measurement

We design liftoff experiments to measure the robot's mean lift force. While we had developed a force sensor for measuring instantaneous aerodynamic forces in previous studies [22], [31], the sensor does not work for this robot because of the high operating frequency. The previous sensor has a structural resonant frequency near 1000 Hz, and previous piezoelectric-driven robots operate in the range of 120 to 200 Hz. This new robot operates at around 500 Hz, and the lift force signal has a base frequency of 1000 Hz because the wing upstroke and down stroke motions are symmetric. Therefore, the sensor resonance coincides with the lift force frequency and we need to develop a new method to measure forces.

In this study, we design and build a pivot balance to measure the robot's mean lift. Fig. 6(a) shows the experimental setup. A lightweight balance beam is installed on the acrylic stand through a thin carbon fiber rod. The beam's own weight is balanced relative to the pivot point. The robot is affixed at one end of the beam at a distance of L_{robot}, and extra payload can be mounted on the beam at a distance of L_{load}. In an experiment, we

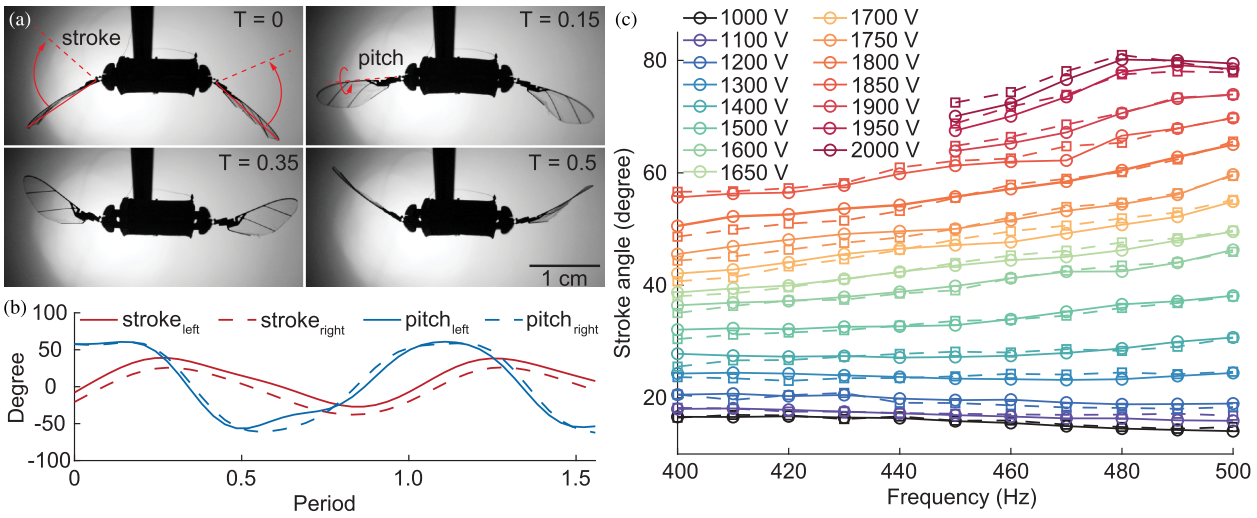

Fig. 5. Characterization of robot flapping wing kinematics. (a) Image sequence showing the robot being operated at 2000 V and 450 Hz. (b) Tracked wing stroke and pitch kinematics of the robot's left and right wings. In (a) and (b), the time is normalized to a flapping period. (c) Wing stroke amplitude as a function of driving frequency and voltage. The solid and dotted lines represent data of the left and the right wings, respectively.

command the robot liftoff and record a video using a high-speed camera (Phantom v710).

Next, we analyze the high-speed video by measuring the beam angle at every image frame, and then estimate the mean lift force by using a simple dynamical model. Fig. 6(b) and (c) shows two liftoff experiments and label the beam angles. When the robot is operated at 2000 V and 450 Hz, the beam angle increases from 5° to 17° in 0.08 s while a 50 mg payload is attached to the balance beam [see Fig. 6(b)]. We conduct several experiments with different payload weights. When the payload increases to 158 mg [see Fig. 6(c)], the beam angle increases from 0.5° to 6.7° in 0.2 s. These experiments are also shown in Supplementary Video 2.

Fig. 6(d) shows the measured beam angle as a function of time for five takeoff experiments. In these experiments, we gradually increase the payload weights from 0 to 158 mg. The robot weighs 164 mg. After tracking the beam angle, we calculate the mean lift force during takeoff by fitting to the equation of motion

$$I_{\text{total}}\ddot{\theta} = (F_{\text{lift}} - m_{\text{fly}}g\cos\theta)L_{\text{fly}} - m_{\text{load}}gL_{\text{load}}\cos\theta. \quad (10)$$

This simple model ignores the friction force due to the rotational motion around the pivot, the drag force as the robot ascends, and the robot's small oscillation along its roll axis. Ignoring these dissipative effects gives a conservative estimate of the robot's mean lift. When the payload is small (0, 50, and 95 mg), these effects are less important, and the beam angle measurement resembles a parabolic profile [red, orange, and yellow curves in Fig. 6(d)]. These higher order effects become apparent when the robot lifts off with a larger payload [green and blue curves in Fig. 6(d)]. Fig. 6(e) lists the mean lift-to-weight ratio calculated from these five experiments. At the robot's peak operating conditions (2000 V, 450–490 Hz), the robot achieves a lift-to-weight ratio of 2.2:1. This result represents a 83% improvement over our previous work [33], and it enables new flight capabilities that will be described in Section IV.

IV. Robot Flight Demonstrations

We fabricate four robot modules and assemble them into an eight-wing robot to demonstrate controlled flights. While the robot configuration is the same as in our previous work [33], this robot can demonstrate new flight capabilities because of its improved net lift. In the following sections, we describe the experimental setup, hovering and ascending flights, in-flight collision recovery demonstrations, and somersault maneuvers.

A. Experimental Setup

To demonstrate controlled flights, we use an existing Vicon motion tracking arena [22]. Four 1.5 mm reflective markers (B&L Engineering) are attached to the robot for position and attitude tracking. The Vicon tracking system has six infrared cameras that operate at 500 Hz, and it has a tracking volume of $40 \times 40 \times 20$ cm. If the robot flies above 20 cm, then only three higher mounted cameras can see the robot and the tracking result becomes error prone. In addition, the system loses tracking when the body pitch or roll angle exceeds 100° because the reflective markers are semispheres and do not reflect infrared signals when flipped upside down.

We use an existing feedback controller [33] to demonstrate hovering flights and in-flight collision recovery. The controller gains are adjusted to account for the new robot's voltage to force mapping. For hovering demonstrations, we use a linear mapping function

$$V_{\text{input}} = V_{\text{takeoff}} + V_{\text{scale}} \times \left(\frac{F_{\text{lift}}}{m_{\text{fly}}g} - 0.2\right). \quad (11)$$

For each robot module, the values of V_{takeoff} and V_{scale} are individually tuned. These values are set based on the liftoff experiments. V_{takeoff} corresponds to the voltage at which the robot lift is equal to its weight. The sum of V_{takeoff} and V_{scale} correspond to the voltages at which the robot lift is 1.2 times

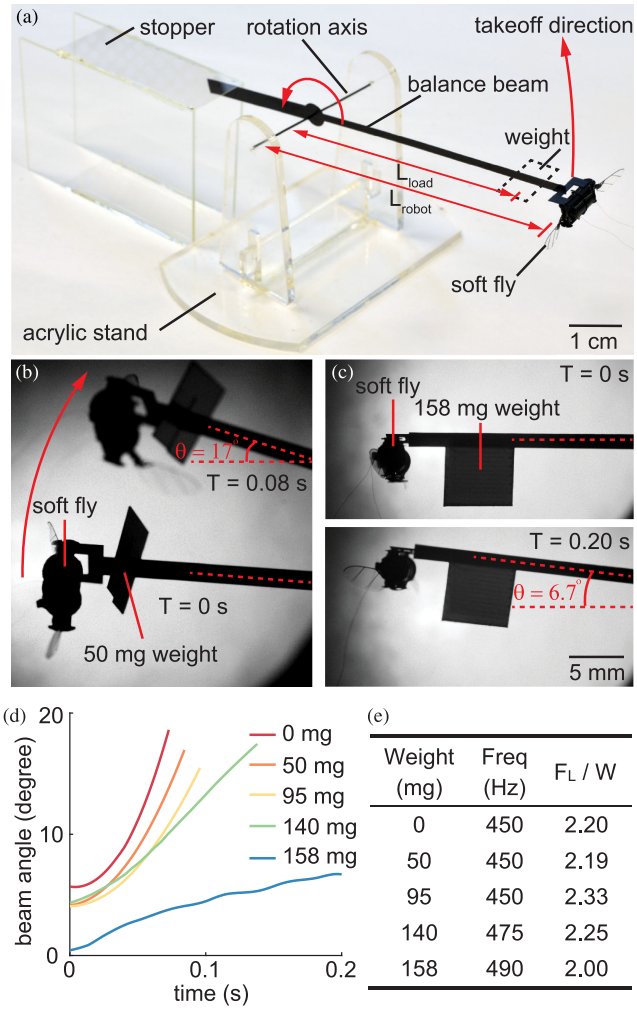

Weight (mg)	Freq (Hz)	F_L / W
0	450	2.20
50	450	2.19
95	450	2.33
140	475	2.25
158	490	2.00

Fig. 6. Robot lift off demonstrations and measurements of the net lift force. (a) Image showing a custom-made pivot balance that is used to measure a robot's net lift. (b) Composite image showing a robot takes off while carrying a 50 mg payload. (c) Two images that show a robot takes off while carrying a 158 mg payload. The beam angle θ is labeled in (b) and (c). (d) Tracked beam angle during five liftoff flights in which the payload mass gradually increases. (e) Table that lists the calculated lift-to-weight ratio for these experiments. The operating frequency in these experiments change slightly in the range of 450 Hz to 490 Hz, and the driving voltage is 2000 V for all cases. The average lift-to-weight ratio is 2.19:1.

the robot weight. Their nominal values are 1700 and 60 V, respectively.

B. Controlled Hovering Flight and Ascending Flight

First, we demonstrate this new robot can achieve controlled hovering flights [see Fig. 7]. Fig. 7(a) shows an image sequence illustrating a 10 s hover, and Fig. 7(b) plots the trajectory of the same experiment. The color scale in Fig. 7(b) represents the distance from the robot to the setpoint. Fig. 7(c)–(e) shows the tracked altitude [see Fig. 7(c)], the robot x and y positions [see Fig. 7(d)], and the body roll and pitch angles [see Fig. 7(d)]. In this 10 s flight, the altitude error is smaller than 0.5 cm and the drift in the *xy* plane is smaller than 4 cm. The robot does not have control of its body yaw rotation. This flight is also shown in Supplementary Video 3.

In addition, we perform controlled ascending flights to demonstrate robot agility [see Fig. 8]. Fig. 8(a) shows a composite image of an ascending flight demonstration. The robot takes off and hovers around a setpoint, and then it ascends upward with a net thrust force that is set to 1.5 times its weight. The net thrust force is used for both altitude acceleration and attitude stabilization. It flies upward until all Vicon cameras lose tracking. Fig. 8(b) shows the tracked robot altitude for this same flight. The red insets in Fig. 8(b) indicate the acceleration and the ascent phases, and these zoomed-in plots are shown in Fig. 8(c) and (d). In Fig. 8(c), we overlay a parabolic fit (red) of the robot acceleration on the measured data (blue). This fit shows the robot accelerates upward with 250 cm/s^2. As the robot flies upward, aerodynamic drag increases and eventually the robot reaches a terminal velocity. Fig. 8(d) overlays a linear fit of the robot's altitude on the measured data. The fit shows the robot's ascending speed reaches 70 cm/s. Compared to our previous work [33], this robot shows an over two times improvement of the maximum ascending speed. To the best of our knowledge, this ascending speed further exceeds that of all rigid-driven subgram MAVs [13-21]. This flight is shown in Supplementary Video 4.

To show flight repeatability, we conduct three experiments with the same control parameters. Fig. 8(e)–(g) shows the robot altitude [see Fig. 8(e)], the x and y positions [see Fig. 8(f)], and the pitch and roll angles [see Fig. 8(g)]. In these plots, the solid lines show the mean of the three trials and the shaded areas illustrate one standard deviation from the mean.

C. In-Flight Collision Recovery

In addition to demonstrating hovering and ascending flights, the new robot can recover from in-flight collisions through feedback control. Although we had shown the previous DEA-driven robot is resilient against collisions [33], the robot was unable to show closed-loop in-flight collision recovery due to having limited lift forces. With substantially higher lift, the new robot demonstrates three collision recovery flights.

In these experiments, we command the robot to hover for 5 s using the same controller described in the previous sections. While the robot hovers around its setpoint, we manually hit the robot with a carbon fiber rod. Fig. 9(a)–(c) shows the first collision recovery demonstration in which we push the robot downward with negligible attitude disturbance. The robot's altitude reduces by 4 cm 0.35 s after it is hit [see Fig. 9(a)]. Then, the robot gradually returns to the hovering setpoint. Fig. 9(b) and (c) shows the robot's altitude, pitch, and roll motion. The red regions highlight the collision recovery phase. This demonstration shows the robot has sufficient control authority (forces and torques) to recover from in-flight disturbances.

The second demonstration [see Fig. 9(d)–(f)] shows collision recovery when an obstacle hits the robot wing. The carbon fiber rod is slowly brought into the flight arena until it hits a robot wing [see Fig. 9(d)]. The collision interferes the flapping kinematics, and it further reduces the instantaneous lift. The controller quickly recovers its attitude, and returns to its hovering setpoint 0.5 s after the collision. Fig. 9(e)–(f) shows the robot's altitude,

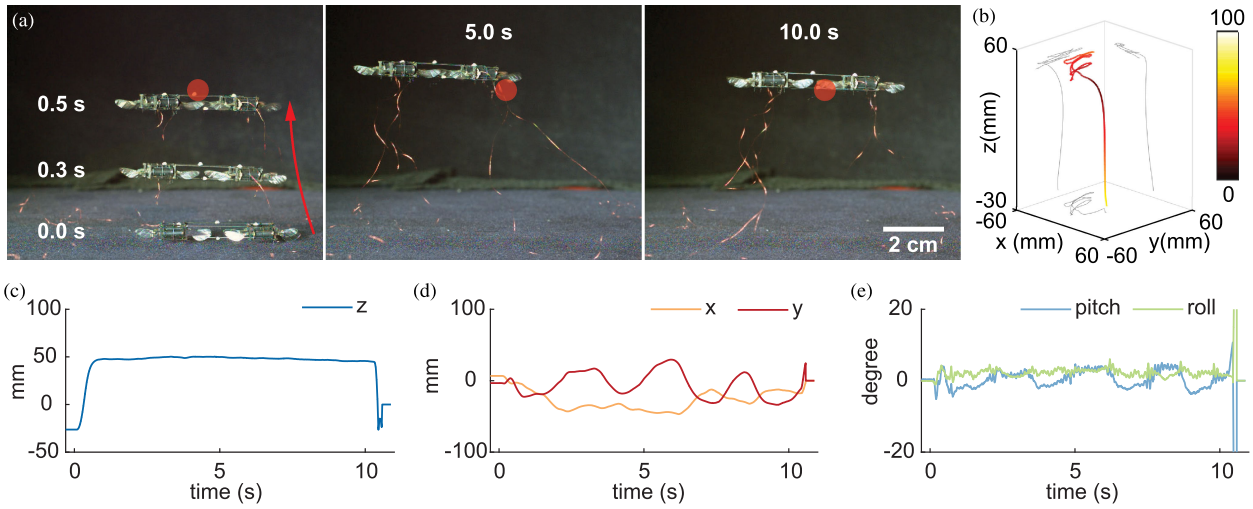

Fig. 7. Robot closed-loop hovering demonstration. (a) Image sequence that shows a 10 s hovering flight. (b) Robot's tracked trajectory that corresponds to the experiment shown in (a). The color scale represents the robot' s distance from the controller setpoint. (c)–(e) Robot's tracked altitude (c), x and y positions (d), and pitch and roll motion (e). The robot does not have control of its body yaw motion. In this experiment, the position setpoint is (0; 0; 50) mm with respect to the motion tracking system's origin. The pitch and roll setpoints are both 0.

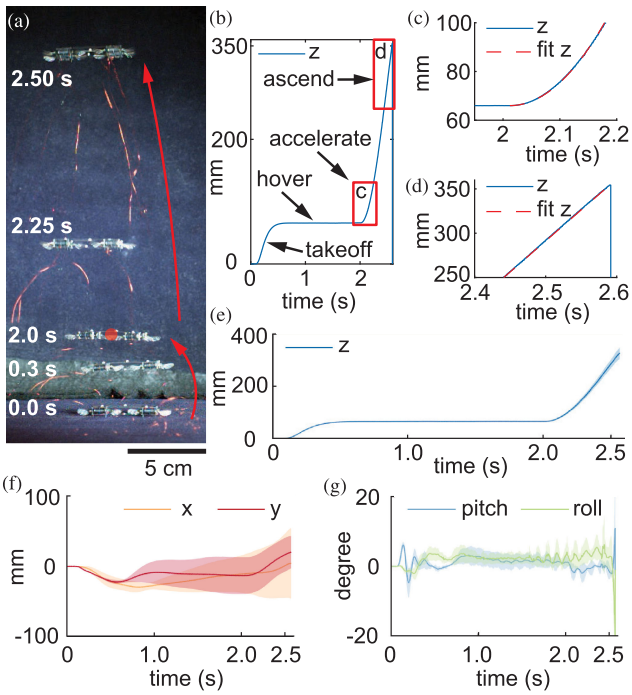

Fig. 8. Robot ascending flight demonstration. (a) Composite image that shows an ascending flight experiment. (b) Robot's tracked altitude that corresponds to the same experiment in (a). (c) Robot acceleration phase that corresponds to the red inset in (b). The parabolic fit shows the robot accelerates upward at 250 cm/s^2. (d) Robot's ascent phase that corresponds to the red inset in (b). Linear fit shows the robot flies upward at a speed of 70 cm/s. (e)–(f) Robot's tracked altitude (c), x and y positions (d), and pitch and roll motion (e) for three ascending flight experiments. The solid lines represent the mean values and the shaded regions represent one standard deviation from the mean.

pitch, and roll motion. This demonstration shows the robot wing, transmission, and actuator are resilient against external impact.

The third demonstration [see Fig. 9(g)–(i)] shows a substantially stronger impact. Fig. 9(g) shows the collision induces a large downward speed and a fast body pitch rotation. The robot hits the ground approximately 0.1 s after the collision. It recovers its attitude after hitting the ground, and eventually returns to the hovering setpoint approximately 1.0 s after the collision. Fig. 9(h) and (i) shows the robot's altitude, pitch, and roll motion. Fig. 9(i) shows the maximum pitch angle is approximately 50°, and the robot can recover after experiencing a large attitude disturbance. These three collision recovery flights are also shown in Supplementary Video 5. This experiment further shows the robot can use the ground to recover from collisions when the motion tracking arena's height is limited. In the following section, we conduct robot somersault demonstrations in this small motion tracking arena. The robot also uses the ground to recover after completing a somersault.

D. Somersault Demonstrations

Collision recovery demonstrations show our robot is robust against collisions and it can generate sufficient forces and torques. In this section, we show somersault maneuvers to illustrate the DEA's high-bandwidth and good controllability. First, we design a closed-loop simulator and manually select control parameters to find a feasible trajectory. Next, we conduct five somersault experiments to demonstrate repeatability.

We develop a robot dynamical model and a feedback controller to design feasible somersault trajectories. Given a setpoint and the robot's instantaneous states (position, attitude, and their derivatives), the controller calculates the control inputs: net thrust force, body pitch torque, and body roll torque. These control inputs are later mapped to the commanding voltage amplitude of each robot actuator. Based on these input signals, our simulator calculates the robot motion and feeds this information back to the controller.

Our somersault simulator consists of five parts: takeoff, ascent, flip, recovery, and hover. During the takeoff phase, the robot lifts off from the ground and hovers around a setpoint for 2 s. Next, the robot accelerates upward with a constant acceleration.

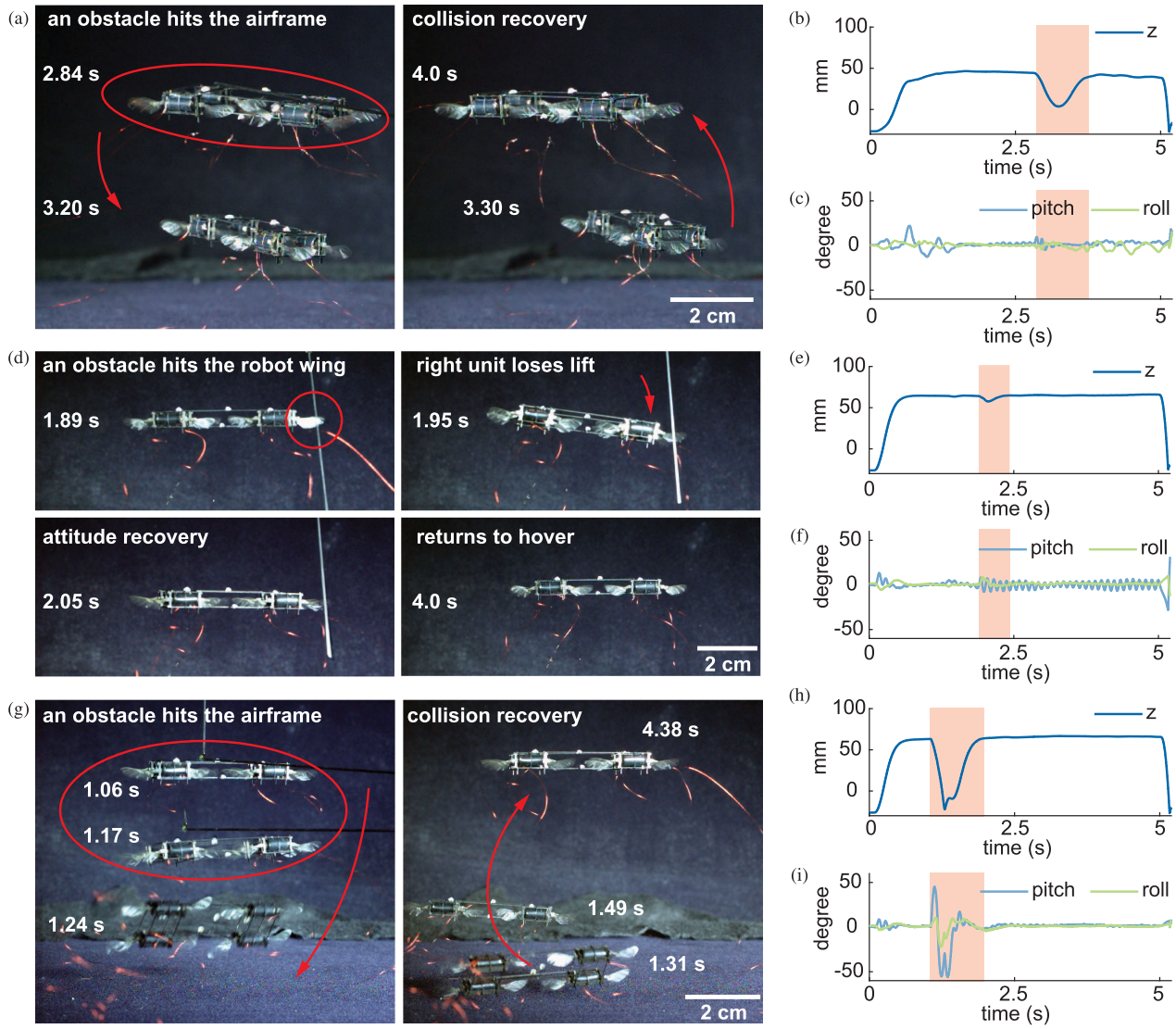

Fig. 9. Three in-flight collision recovery demonstrations. (a) Composite images showing an obstacle hits the robot airframe during hovering flight. The robot recovers to its setpoint 1 s after the collision. (b)–(c) Tracked robot altitude (b) and pitch and roll motion (c) that correspond to the experiment shown in (a). (d) Another collision recovery experiment in which an obstacle hits the robot wing. (e)–(f) Tracked altitude (e) and pitch and roll motion (f) corresponding to (d). (g) Collision recovery experiment in which a large collisional impact induces a large rotational speed and a large downward speed. The robot bounces on the ground and returns to its hovering setpoint. (h)–(i) Tracked altitude (h) and pitch and roll motion (i) corresponding to (g). In (b)–(c), (e)–(f), and (h)–(i), the shaded regions indicate the collision recovery phase.

During this ascending flight, the controller directly sets the net thrust force and ignores requirements on altitude and ascending speed. After accelerating upward for 0.5 s, the robot conducts a somersault maneuver. During this phase, the controller directly sets the body pitch torque and ignores the setpoint position and velocity. The flip phase is split into rotational acceleration and deceleration phases so that the robot stops its pitch rotation after completing the somersault. When the robot performs the somersault, we use a quadratic force to voltage mapping instead of the linear mapping for hovering flights. This quadratic model is more accurate when the controller commands large changes of thrust forces. During hovering flights, the commanding lift mostly varies between 1 to 1.2 times the robot weight. During the rotational acceleration and deceleration phases in a somersault, the commanding lift force of each robot module quickly varies between 0 and 2 times the robot weight. After completing the flip, the controller enters the recovery phase. During this phase, the controller prioritizes attitude stabilization and dynamically updates the setpoint position and velocity such that the robot gradually returns to its original setpoint. Finally, the robot returns to its hovering state and hovers around the setpoint for the reminder of the flight. Table I summarizes all the control parameters used in a 5-s somersault demonstration. In Table I, $\bar{r_d}$ and $\dot{\bar{r}}_d$ are the desired robot position and velocity, $\bar{r}$ and $\dot{\bar{r}}$ are the simulated robot position and velocity, and $\triangle t$ is the amount of time into the recovery phase.

Fig. 10 shows the simulation result of a somersault flight based on the controller parameters shown in Table I. Fig. 10(a) plots the flight trajectory and illustrates the robot's position and orientation at specific times. Fig. 10(b) zooms into the inset

TABLE I
CONTROLLER PARAMETERS USED FOR THE ROBOT SOMERSAULT SIMULATION. THE CONTROLLER HAS FIVE PHASES: TAKEOFF, ASCENT, FLIP, RECOVERY, AND HOVER.

	Time (s)	Setpoints		Control inputs			Force to voltage mapping
		Position (m)	Velocity (m/s)	Net thrust (F/mg)	Pitch torque (Nm)	Roll torque (Nm)	V_t: takeoff voltage V_s: linear voltage scaling V_q: quadratic voltage scaling
Takeoff and hover	2	[0; 0; 0.07]	[0; 0; 0]	--	--	--	$V = V_t + V_s \times (\frac{F_{lift}}{mg} - 0.2)$
Ascent	0.5	[0; 0; NA]	[0; 0; NA]	1.1	--	--	$V = V_t + V_s \times (\frac{F_{lift}}{mg} - 0.2)$
Flip	t_{acc}=0.09 t_{dcc}=0.09	[NA; NA; NA]	[NA; NA; NA]	-- --	5 x 10^5 -5 x 10^5	-- --	$V = V_q \times \sqrt{\frac{F_{lift}}{mg}}$
Recovery	1	$\overline{r_d} + (\frac{\Delta t}{t_r})(\overline{r} - \overline{r_d})$	$\dot{\overline{r_d}} + (\frac{\Delta t}{2t_r})(\dot{\overline{r}} - \dot{\overline{r_d}})$	--	--	--	$V = V_t + V_s \times (\frac{F_{lift}}{mg} - 0.2)$
Hover	1.32	[0; 0; 0.07]	[0; 0; 0]	--	--	--	$V = V_t + V_s \times (\frac{F_{lift}}{mg} - 0.2)$

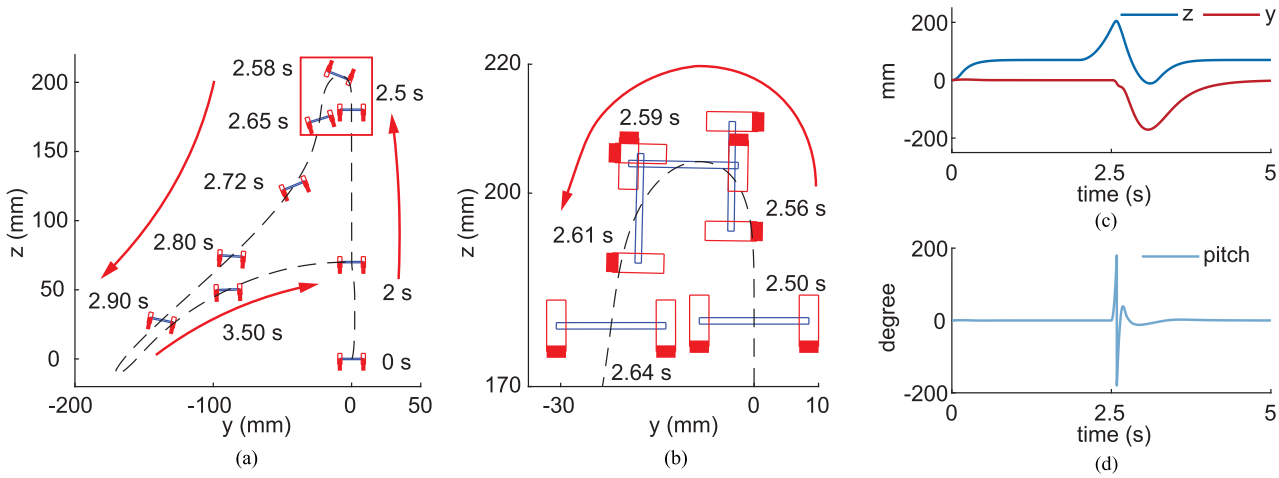

Fig. 10. Simulation of robot somersault flight. (a) Simulated robot somersault flight trajectory (dotted line). The robot's position and attitude are shown for several timepoints. (b) Zoomed-in robot trajectory and attitude during the somersault maneuver. This plot corresponds to the inset in (a). (c) Simulated robot altitude and y position. (d) Simulated robot pitch motion.

highlighted in Fig. 10(a), and it shows the somersault maneuver in detail. The robot makes a complete turn in 0.14 s. Fig. 10(c) plots the robot's y and z motion, and Fig. 10(d) plots the robot's pitch rotation. In this simulation, the robot does not experience external disturbances. Due to the symmetry, the robot's displacement in the x-direction and its roll angle remain zero. While this simulation suggests that a somersault demonstration is feasible, this result does not account for several constraints. First, the motion tracking arena has a limited volume. The robot may be unable to recover its altitude before hitting the ground. Second, the Vicon system loses tracking when the robot flips upside down, and this makes flight recovery difficult. Third, we do not have accurate aerodynamic models of robot drag forces when the robot accelerates upward or flips at a high rotational speed. Due to the drag forces, the flipping time t_{acc} and t_{dcc} need not be identical in a flight experiment.

We perform several trimming flights prior to conducting somersault demonstrations. We find that several controller parameters need to be modified to account for these effects. For instance, the net lift force during robot ascent is increased to 1.2 times (as supposed to the simulation parameter 1.1 listed in Table I) the robot weight because of the aerodynamic drag and the need of larger control torques to stabilize attitude. To account for the large effect of aerodynamic drag during somersault, t_{acc} and t_{dcc} are set to 0.12 and 0.04 s, respectively. Fig. 11(a)–(d) shows a sample somersault demonstration. Fig. 11(a) shows an image sequence illustrating the five phases. The robot takes off and hovers, accelerates upward, flips along its body pitch axis, recovers attitude, and finally returns to hover. Fig. 11(a) shows the robot uses 0.16 s to complete a 360° flip. However, the robot is unable to recover its altitude before hitting the ground. Instead, the robot bounces on the ground and then returns to hovering flight. Fig. 11(b)–(d) shows the robot's altitude, x and y positions, and roll and pitch motion during this flight. The red colored regions indicate the time at which the Vicon system loses tracking. During the body flip, the Vicon system loses tracking for approximately 0.1 s. This flight is also shown in Supplementary Video 6.

Although hitting the ground causes a moderate disturbance, the robot quickly stabilizes its attitude and returns to hovering

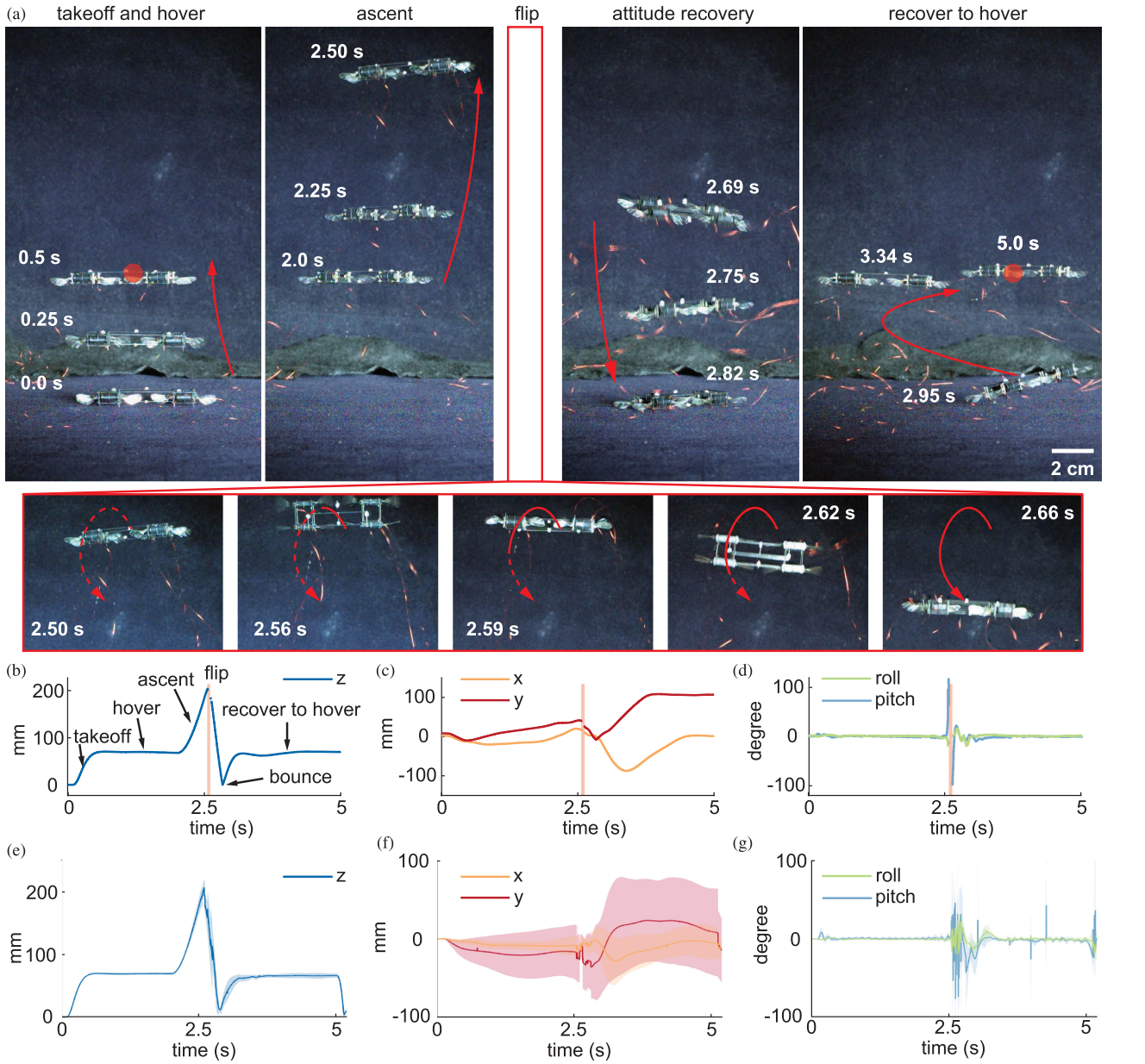

Fig. 11. Robot somersault flight demonstrations. (a) Sequence of composite images that show a 5 s somersault flight. The images illustrate the five flight phases: takeoff, ascent, flip, recovery, and hover. (b)–(d) Tracked robot altitude (b), x and y positions (c), and roll and pitch motions (d) that correspond to the flight shown in (a). The shaded region indicates the time during which the Vicon system loses tracking. (e)–(g) Tracked robot altitude (e), x and y positions (f), and roll and pitch motions (g) of five somersault experiments. The solid line represents the mean value and the shaded regions represent one standard deviation from the mean.

flight. This demonstration shows the robot is both agile and robust. To demonstrate repeatability, we conduct five somersault flights and show these results in Fig. 11(e)–(g). Similar to Fig. 11(b)–(d), these plots show the robot's altitude [see Fig. 11(e)], x and y positions [see Fig. 11(f)], and body roll and pitch motions [see Fig. 11(g)] during these somersault flights. The solid colors represent the mean trajectory, and the shaded regions represent one standard deviation from the mean. These demonstrations show the robot can reliably perform somersaults and recover after bouncing off the ground.

Somersault demonstrations require a DEA to handle large instantaneous changes of input signals. During hovering flights, the DEA's input voltage amplitude varies slowly around the hovering conditions (±20 V). In contrast, during the quick body flip, the DEA's voltage amplitude drops from nearly 2000 V to less than 200 V in 2–3 wing beats (<60 ms). This type of driving commands is unfavorable for piezoelectric actuators because it induces a large instantaneous strain, and this can cause the rigid actuator to crack [42]. Here, we show for the first time that a soft-driven robot can perform agile tasks that a rigid-driven robot has not yet demonstrated, and this shows the promise of future soft robotic systems.

V. Conclusion

To summarize, we develop a 665 mg soft aerial robot that can demonstrate robust and agile flights. Specifically, we make a new DEA that shows an 100% increase of output power density

and 560% improvement of transduction efficiency. The DEA is installed into a robot and we further redesign main components including transmission, wing hinges, and wings. The new robot demonstrates a 2.2:1 lift-to-weight ratio, which represents an 83% increase compared to our previous work [33]. In addition to demonstrating hovering flights, this robot shows an ascending speed of 70 cm/s, which exceeds all existing subgram MAVs. Furthermore, we show the robot can demonstrate in-flight collision recovery and aggressive maneuvers such as a somersault. We show for the first time that soft-actuated subgram MAVs can demonstrate robust and agile flight capabilities that the state-of-the-art rigid subgram MAVs have not yet achieved, and this shows the promise of future dynamic soft robotic systems.

While our work shows substantial improvements and enables new flight capabilities, there are several areas that still need to be addressed. To improve the somersault demonstration, we need to expand the motion tracking arena and enable continuous tracking when the robot flips upside down. The existing tracking system is constructed for hovering demonstration and, thus, has a limited tracking volume. Increasing the tracking volume requires us to increase the number of Vicon cameras. To mitigate the loss of tracking when the robot flips upside down, we need to replace the existing reflective markers with ones that are spherical.

More importantly, there are several longer-term directions that future studies need to address. First, achieving power-autonomous flight in subgram soft-actuated MAVs is a grand challenge. Reaching this goal requires compact power electronics and power dense and efficient soft actuators. This work contributes to developing power-dense soft actuators and further incorporating them into a high-lift MAV. Having a 2.2:1 lift-to-weight ratio implies the robot can carry a payload that is approximately equal to its weight. This 500–600 mg payload can be used to carry a battery and power circuitry. Based on preliminary calculation, we estimate that off-the-shelf lithium polymer (Li-Po) batteries can offer enough energy to power flight for 10–30 s (e.g., A 390 mg, 3.7 V, 12 mAh Li-Po battery [41] has 160 J of energy and our robot consumes 1.2 W when driven at maximum lift conditions). In our view, the main challenge involves building lightweight (100–200 mg) power electronics that can efficiently ($>$10%) boost the low battery voltage to a high voltage that can drive the DEAs. One major disadvantage of our current work is the DEA requires a 2000 V driving voltage, which is 10 times higher than piezoelectric actuators. Considering the small robot size and payload, it is difficult to develop power electronics that satisfy the abovementioned requirements. Future studies should reduce the operation voltage by decreasing the elastomer layer thickness. This can be achieved by either increasing the spin coating speed or exploring alternative methods [43] such as doctor blading. In the DEA fabrication process, the elastomer thickness can be reduced to within 10 μm through using prestraining techniques [44]. Besides from working towards power-autonomous flights, future studies should also improve the soft aerial robot's control authority. This study linearizes the DEA actuation and each two-wing robot module alone cannot generate control torques. Consequently, the current robot cannot demonstrate yaw control. Future studies should develop nonlinear DEA models that exploit a DEA's higher harmonic components to generate asymmetric upstroke and down stroke motions. We expect quantifying a DEA's nonlinear dynamics will substantially improve a soft aerial robot's controllability and further enable yaw control. We envision future soft-driven aerial robots will achieve insect-like flight capabilities and will find realistic applications such as environmental exploration.

ACKNOWLEDGMENT

The authors would like to thank Prof. J. Wang for insightful discussion about the robot design and characterization and also like to thank Prof. R. J. Wood for providing equipment and space. All flight experiments were conducted at the Harvard Microrobotics Laboratory.

REFERENCES

[1] P. Liu, S. P. Sane, J.-M. Mongeau, J. Zhao, and B. Cheng, "Flies land upside down on a ceiling using rapid visually mediated rotational maneuvers," *Sci. Adv.*, vol. 5, no. 10, 2019, Art. no. eaax 1877.

[2] A. K. Dickerson, P. G. Shankles, N. M. Madhavan, and D. L. Hu, "Mosquitoes survive raindrop collisions by virtue of their low mass," *in Proc. Nat. Acad. Sci.*, vol. 109, no. 25, pp. 9822–9827, 2012.

[3] A. M. Mountcastle and S. A. Combes, "Biomechanical strategies for mitigating collision damage in insect wings: Structural design versus embedded elastic materials," *J. Exp. Biol.*, vol. 217, no. 7, pp. 1108–1115, 2014.

[4] B. Michini, J. Redding, N. K. Ure, M. Cutler, and J. P. How, "Design and flight testing of an autonomous variable-pitch quadrotor," in *Proc. IEEE Int. Conf. Robot. Autom.*, 2011, pp. 2978–2979.

[5] D. Mellinger, N. Michael, and V. Kumar, "Trajectory generation and control for precise aggressive maneuvers with quadrotors," *Int. J. Robot. Res.*, vol. 31, no. 5, pp. 664–674, 2012.

[6] S. Lupashin, A. Schöllig, M. Sherback, and R. D'Andrea, "A simple learning strategy for high-speed quadrocopter multi-flips," in *Proc. IEEE Int. Conf. Robot. Autom.*, 2010, pp. 1642–1648.

[7] J. H. Gillula, H. Huang, M. P. Vitus, and C. J. Tomlin, "Design of guaranteed safe maneuvers using reachable sets: Autonomous quadrotor aerobatics in theory and practice," in *Proc. IEEE Int. Conf. Robot. Autom.*, 2010, pp. 1649–1654.

[8] A. Briod, P. Kornatowski, J.-C. Zufferey, and D. Floreano, "A collision-resilient flying robot," *J. Field Robot.*, vol. 31, no. 4, pp. 496–509, 2014.

[9] S. Mintchev, J. Shintake, and D. Floreano, "Bioinspired dual-stiffness origami," *Sci. Robot.*, vol. 3, no. 20, 2018, Art. no. eaau0275.

[10] P. Sareh, P. Chermprayong, M. Emmanuelli, H. Nadeem, and M. Kovac, "Rotorigami: A rotary origami protective system for robotic rotorcraft," *Sci. Robot.*, vol. 3, no. 22, 2018. Art. no. eaah5228.

[11] J. Shu and P. Chirarattananon, "A quadrotor with an origami-inspired protective mechanism," *IEEE Robot. Autom. Lett.*, vol. 4, no. 4, pp. 3820–3827, Oct. 2019.

[12] Z. Tu, F. Fei, J. Zhang, and X. Deng, "Acting is seeing: Navigating tight space using flapping wings," in *Proc. Int. Conf. Robot. Automat.*, 2019, pp. 95–101.

[13] Y.-W. Chin *et al.*, "Efficient flapping wing drone arrests high speed flight using post-stall soaring," *Sci. Robot.*, vol. 5, 2020, Art. no. eaba 2386.

[14] M. Karásek, F. T. Muijres, C. De Wagter, B. D. Remes, and G. C. de Croon, "A tailless aerial robotic flapper reveals that flies use torque coupling in rapid banked turns," *Science*, vol. 361, no. 6407, pp. 1089–1094, 2018.

[15] Z. Tu, F. Fei, J. Zhang, and X. Deng, "An at-scale tailless flapping-wing hummingbird robot. i design, optimization, and experimental validation," *IEEE Trans. Robot.*, vol. 36, no. 5, pp. 1511–1525, Oct. 2020.

[16] H. V. Phan and H. C. Park, "Design and evaluation of a deformable wing configuration for economical hovering flight of an insect-like tailless flying robot," *Bioinspiration Biomimetics*, vol. 13, no. 3, 2018, Art. no. 036009.

[17] F. Fei, Z. Tu, J. Zhang, and X. Deng, "Learning extreme hummingbird maneuvers on flapping wing robots," in *Proc. Int. Conf. Robot. Automat.*, 2019, pp. 109–115.

[18] H. V. Phan and H. C. Park, "Mechanisms of collision recovery in flying beetles and flapping-wing robots," *Science*, vol. 370, no. 6521, pp. 1214–1219, 2020.

[19] X. Yang, L. Chang, and N. O. Pérez-arancibia, "An 88-milligram insect-scale autonomous crawling robot driven by a catalytic artificial muscle," *Sci. Robot.*, vol. 5, no. 45, 2020 Art. no. eaba0015.

[20] Y. Wu *et al.*, "Insect-scale fast moving and ultrarobust soft robot," *Sci. Robot.*, vol. 4, no. 32, 2019, Art. no. eaax 1594 .
[21] N. T. Jafferis, M. J. Smith, and R. J. Wood, "Design and manufacturing rules for maximizing the performance of polycrystalline piezoelectric bending actuators," *Smart Mater. Structures*, vol. 24, no. 6, 2015, Art. no. 065023.
[22] K. Y. Ma, P. Chirarattananon, S. B. Fuller, and R. J. Wood, "Controlled flight of a biologically inspired, insect-scale robot," *Science*, vol. 340, no. 6132, pp. 603–607, 2013.
[23] E. F. Helbling, S. B. Fuller, and R. J. Wood, "Altitude estimation and control of an insect-scale robot with an onboard proximity sensor," in *Proc. Robot. Res*., Berlin, Germany, Springer, 2018, pp. 57–69.
[24] J. James, V. Iyer, Y. Chukewad, S. Gollakota, and S. B. Fuller, "Liftoff of a 190 mg laser-powered aerial vehicle: The lightest wireless robot to fly," in *Proc. IEEE Int. Conf. Robot. Autom.*, 2018, pp. 1–8.
[25] N. T. Jafferis, E. F. Helbling, M. Karpelson, and R. J. Wood, "Untethered flight of an insect-sized flapping-wing microscale aerial vehicle," *Nature*, vol. 570, no. 7762, pp. 491–495, 2019.
[26] M. Graule *et al.*, "Perching and takeoff of a robotic insect on overhangs using switchable electrostatic adhesion," *Science*, vol. 352, no. 6288, pp. 978–982, 2016.
[27] P. Chirarattananon, K. Y. Ma, and R. J. Wood, "Adaptive control of a millimeter-scale flapping-wing robot," *Bioinspiration Biomimetics*, vol. 9, no. 2, 2014, Art. no. 025004.
[28] Y. Chen *et al.*, "A biologically inspired, flapping-wing, hybrid aerial-aquatic microrobot," *Sci. Robot.*, vol. 2, no. 11, 2017, Art. no. eaao5619.
[29] S. B. Fuller, "Four wings: An insect-sized aerial robot with steering ability and payload capacity for autonomy," *IEEE Robot. Autom. Lett.*, vol. 4, no. 2, pp. 570–577, Apr. 2019.
[30] X. Yang, Y. Chen, L. Chang, A. A. Calderón, and N. O. Pérez-Arancibia, "Bee : A 95-mg four-winged insect-scale flying robot driven by twinned unimorph actuators," *IEEE Robot. Autom. Lett.*, vol. 4, no. 4, pp. 4270–4277, Oct. 2019.
[31] Y. Chen, K. Ma, and R. J. Wood, "Influence of wing morphological and inertial parameters on flapping flight performance," in *Proc. IEEE/RSJ Int. Conf. Intell. Robots Syst.* , 2016, pp. 2329–2336.
[32] A. M. Mountcastle, E. F. Helbling, and R. J. Wood, "An insect-inspired collapsible wing hinge dampens collision-induced body rotation rates in a microrobot," *J. Roy. Soc. Interface*, vol. 16, no. 150, 2019, Art. no. 20180618.
[33] Y. Chen *et al.*, "Controlled flight of a microrobot powered by soft artificial muscles," *Nature*, vol. 575, no. 7782, pp. 324–329, 2019.
[34] H. Zhao, A. M. Hussain, M. Duduta, D. M. Vogt, R. J. Wood, and D. R. Clarke, "Compact dielectric elastomer linear actuators," *Adv. Funct. Mater.*, vol. 28, no. 42, 2018, Art. no. 1804328.
[35] Y. Bar-Cohen, *Electroactive Polymer (EAP) Actuators as Artificial Muscles: Reality, Potential, and Challenges*, vol. 136. Bellingham, WA, USA: SPIE, 2004.
[36] J. Huang, S. Shian, R. M. Diebold, Z. Suo, and D. R. Clarke, "The thickness and stretch dependence of the electrical breakdown strength of an acrylic dielectric elastomer," *Appl. Phys. Lett.*, vol. 101, no. 12, 2012, Art. no. 122905.
[37] J. Huang, S. Shian, Z. Suo, and D. R. Clarke, "Maximizing the energy density of dielectric elastomer generators using equi-biaxial loading," *Adv. Funct. Mater.*, vol. 23, no. 40, pp. 5056–5061, 2013.
[38] F. Carpi, P. Chiarelli, A. Mazzoldi, and D. De Rossi, "Electromechanical characterisation of dielectric elastomer planar actuators: Comparative evaluation of different electrode materials and different counterloads," *Sensors Actuators A, Phys.*, vol. 107, no. 1, pp. 85–95, 2003.
[39] C. Keplinger, J.-Y. Sun, C. C. Foo, P. Rothemund, G. M. Whitesides, and Z. Suo, "Stretchable, transparent, ionic conductors," *Science*, vol. 341, no. 6149, pp. 984–987, 2013.
[40] L. J. Romasanta, M. A. López-Manchado, and R. Verdejo, "Increasing the performance of dielectric elastomer actuators: A review from the materials perspective," *Prog. Polym. Sci.*, vol. 51, pp. 188–211, 2015.
[41] X. Ji *et al.*, "An autonomous untethered fast soft robotic insect driven by low-voltage dielectric elastomer actuators," *Sci. Robot.*, vol. 4, no. 37, 2019, Art. no. eaaz6451.
[42] R. J. Wood, E. Steltz, and R. Fearing, "Optimal energy density piezoelectric bending actuators," *Sensors Actuators A, Phys.*, vol. 119, no. 2, pp. 476–488, 2005.
[43] S. Rosset, O. A. Araromi, S. Schlatter, and H. R. Shea, "Fabrication process of silicone-based dielectric elastomer actuators," *J. Visualized Exp.*, no. 108, 2016, Art. no. e53423.
[44] S. J. A. Koh *et al.*, "Mechanisms of large actuation strain in dielectric elastomers," *J. Polym. Sci. B, Polym. Phys.*, vol. 49, no. 7, pp. 504–515, 2011.

YuFeng Chen (Member, IEEE) received the B.S. degree in applied and engineering physics from Cornell University, Ithaca, NY, USA, in 2012, and the Ph.D. degree in engineering sciences from Harvard University, Cambridge, MA, USA, in 2017.

He is currently a D. Reid Weedon, Jr. '41 Career Development Assistant Professor with the Department of Electrical Engineering and Computer Science, Massachusetts Institute of Technology, USA. His research interests include flapping-wing aerodynamics, microrobotics, soft robotics, and applications of dynamics and control.

Siyi Xu (Student Member, IEEE) received the B.S. degree in material science and engineering from the University of Illinois at Champaign-Urbana, Champaign-Urbana, IL, USA, in 2016, and the M.S. degree in engineering science from Harvard University, Cambridge, MA, USA, in 2018. She is currently working toward the Ph.D. degree in soft robotics, focusing on wearable biocompatible soft sensors and dielectric elastomer actuators with the Harvard Microrobotics Lab, Harvard University, Cambridge, MA, USA.

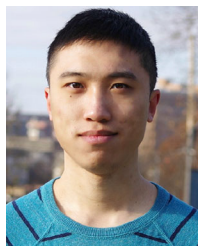

Zhijian Ren (Student Member, IEEE) received the B.S. degree in automation from Shanghai Jiao Tong University, Shanghai, China, and the M.S. degree in mechanical engineering from Carnegie Mellon University, Pittsburgh, PA, USA. He is currently working toward the Ph.D. degree in soft and bio-inspired robotics with the Department of Electrical Engineering and Computer Science, Massachusetts Institute of Technology.

He currently works with Prof. Y. (Kevin) Chen at Soft and Micro Robotics Laboratory, focusing on the actuation, sensing, and control of micro flying robots.

Pakpong Chirarattananon (Member, IEEE) received the B.A. degree in natural sciences from the University of Cambridge, Cambridge, U.K., in 2009, and the Ph.D. degree in engineering sciences from Harvard University, Cambridge, MA, USA, in 2014.

He is currently an Associate Professor with the Department of Biomedical Engineering, City University of Hong Kong, Hong Kong, SAR, China. His research interests include bioinspired robots, micro air vehicles, and the applications of control and dynamics in robotic systems.